


DEFORMATION AND TRANSITIONS AT GRAIN BOUNDARIES

Interface Facilitated Reorientation of Mg Nanolayers in Mg-Nb Nanolaminates

Y. CHEN^{1,2,5}  M.Y. GONG,³ S. SHAO,⁴ N.A. MARA,¹ and J. WANG^{3,6}

1.—Department of Chemical Engineering and Materials Science, University of Minnesota, Minneapolis, MN 55455, USA. 2.—Department of Mechanical Engineering, University of North Carolina at Charlotte, Charlotte, NC 28223, USA. 3.—Mechanical and Materials Engineering, University of Nebraska-Lincoln, Lincoln, NE 68588, USA. 4.—Department of Mechanical and Industrial Engineering, Louisiana State University, Baton Rouge, LA 70803, USA. 5.—e-mail: ychen103@uncc.edu. 6.—e-mail: jianwang@unl.edu

Mg/Nb nanolaminates synthesized through vapor deposition techniques exhibit high flow strength without conventional twinning in Mg. In this work, we investigated the influence of laminated microstructures on deformation mechanisms of Mg nanolayers. Using molecular dynamics simulations, we explored that (0001)-oriented Mg layers transform or re-orient to {10 $\bar{1}$ 0}-oriented Mg layers through nucleation and growth of {10 $\bar{1}$ 2} twins by atomic shuffling, instead of conventional {10 $\bar{1}$ 2} twinning shear. Such a reorientation accommodates in-plane compressive strain and out-of-plane tensile strain when Mg/Nb laminates are subjected to compression parallel to the Mg/Nb interfaces. The nucleation of {10 $\bar{1}$ 2} twins is promoted at the Mg/Nb interface due to the structural change associated with the glide of interface dislocations. The growth of {10 $\bar{1}$ 2} twins is accomplished through migration of basal-prismatic boundaries via nucleation and glide of one-layer and two-layer disconnections associated with atomic shuffling. The results shed light on improving mechanical properties of hexagonal close-packed metals employing laminated structures.

INTRODUCTION

Mg and Mg alloys with a hexagonal close-packed (HCP) structure exhibit low strength, very limited formability and strong plastic anisotropy at room temperature^{1–4} because of the easy-glide basal slip and deformation twinning. Basal slip does not contribute to plastic deformation along the $\langle c \rangle$ -axis. Non-basal slip accommodates plastic deformation along the $\langle c \rangle$ -axis but is rarely activated due to high frictional forces and low mobility.^{5–7} Alternatively, unidirectional shear localization associated with twinning is activated to accommodate deformation along the $\langle c \rangle$ -axis.⁸ It has been observed that microcracking in HCP metals is prone to nucleation at the intersections between deformation twins and free surfaces, grain boundaries or other twins, due to high stress concentrations at the intersections^{3,9,10} and the ineffective accommodation of plastic deformation, i.e., one twin cannot transmit into the other

one.¹¹ Improvement of mechanical properties of Mg and Mg alloys can be achieved through tailoring the relative activity among basal slip, non-basal slip and twinning.

Processing at elevated temperatures,^{12–14} alloying with appropriate elements,^{15,16} refining grain sizes,^{17–19} and weakening crystallographic textures^{20,21} have all been demonstrated to effectively enhance mechanical behavior to some extent. Processing at elevated temperatures can enhance the activity of non-basal slip while lowering twinning activity. Alloying with rare-earth elements is very effective in enhancing the activity of non-basal slips,^{15,16} weakening basal textures,^{20,21} and forming long-period stacking-ordered (LPSO) structures or a high density of stacking faults (SFs).^{22,23} High-density SFs and LPSO structures provide ample barriers to block and pin dislocations and twins, promoting dislocation accumulation and work hardening.²⁴ Apart from these aforementioned approaches,

nanolayered composites containing a high density of heterophase interfaces which control the nucleation and motion of dislocations could make HCP metals strong and ductile.^{25–30} Using accumulative roll bonding, Zr layers in Zr/Nb laminates were successfully refined to ~ 90 nm, and deformation twinning was effectively suppressed.³¹ Ham and Zhang deposited Mg/Nb multilayers with individual layer thicknesses in the range of 2.5–200 nm. The mechanical strength inferred from indentation hardness can be as high as 0.8 GPa when the layers are a few nanometers thick.³² Pathak et al.³³ also demonstrated an extremely high peak strength of 1.7 GPa of Mg/Nb multilayers with an individual layer thickness of 50 nm by micro-pillar compression.

In vapor-deposited Mg/Nb nanolaminates, the Mg/Nb is comprised of the (0001) plane of Mg and the (110) plane of Nb, i.e., $\{0001\}_{\text{Mg}} \parallel \{110\}_{\text{Nb}}$ interfaces.^{32,34–36} In the interface plane, the [1120] and $[\bar{1}100]$ directions of Mg are parallel to the [001] and $[\bar{1}10]$ directions of Nb, respectively. When the loading is normal or parallel to the interface, basal slip will be suppressed due to the zero Schmid factor while non-basal slip and deformation twinning could be activated in Mg.^{37,38} However, twinning might be constrained due to the incompatibility of plastic deformation between Mg and Nb layers, because localized slip/twin bands in Nb are difficult to form. The back stress due to the geometric and elastic/plastic constraints of the adjacent Nb layers will impede nucleation and thickening of twins in the Mg layer, limiting the overall extent of deformation twinning.

In this work, we report on the influence of a nano-laminate microstructure on the deformation mechanisms in Mg nanolayers based on molecular dynamics simulations of Nb/Mg/Nb sandwich structures. The Mg nanolayer deforms through a martensitic transformation mechanism, generating expansion and compression in two orthogonal directions. Mg/Nb interfaces act as nucleation sites and promote this transformation. The results shed light on improving the mechanical properties of HCP metals when a constituent in laminated structures.

ATOMISTIC SIMULATIONS

Molecular dynamics (MD) simulations were carried out on a Nb/Mg/Nb sandwich using the embedded atom method interatomic potentials for Mg,³⁹ Nb⁴⁰ and their cross-pairs.³⁵ The Mg/Nb layers adopt the orientation relationship $(0001) \parallel (01\bar{1})$ and $[2\bar{1}\bar{1}0] \parallel [100]$, as observed in Mg/Nb multilayers.³⁵ The Nb/Mg/Nb sandwich has dimensions of 35.5 nm and 9.9 nm in the x and z directions, respectively. In the simulations, the Mg layer is ~ 5.6 nm thick and sandwiched by two Nb layers with a thickness of ~ 6.4 nm. The x -axis is along $[01\bar{1}0]$ for Mg and $[011]$ for Nb, the z -axis is along

$[2\bar{1}\bar{1}0]$ for Mg and $[100]$ for Nb, and the y -axis (normal of interface plane) is along $[0001]$ for Mg and $[01\bar{1}]$ for Nb. Periodic boundary conditions are applied in the x -, y - and z -directions. MD simulations were performed at temperature $T = 300$ K which was controlled using a nose–hoover thermal bath.^{41,42} Uniaxial loading along the x -axis was simulated by applying a constant strain rate $\dot{\epsilon}_{11} = -2.5 \times 10^8/\text{s}$, while dynamic boundary conditions were applied for the y and z axes to achieve uniaxial compressive stress along the x -axis.⁴³

RESULTS AND DISCUSSION

Under compressive straining along the x -axis, Fig. 1 reveals the deformation process in the Mg layer. One subdomain in the Mg layer (Fig. 1b) is nucleated from the Mg/Nb interface at a compressive strain of $\epsilon_{11} = -5\%$. The nucleus grows and approaches another interface, as shown in Fig. 1c. Once the domain impinges the second interface, the domain grows transversely along the z -axis in the Mg layer (Fig. 1d, e). At a strain of $\epsilon_{11} = -5.5\%$, another subdomain in Fig. 1c is nucleated from the interface and grows via the same mechanism. Once the domain grows through the thickness of the model (z -direction), the domain grows primarily through the migration of basal–prismatic boundaries. Two domains grow, meet and coalesce at $\epsilon_{11} = -6.25\%$. The Mg layer is reoriented from the basal orientation to the prismatic orientation (Fig. 1f), rotating 90° about the z -axis. The Mg/Nb interfaces remain atomically flat, but the orientation relationship changes from $(0001)_{\text{Mg}} \parallel (01\bar{1})_{\text{Nb}}$ and $[2\bar{1}\bar{1}0]_{\text{Mg}} \parallel [100]_{\text{Nb}}$ to $(10\bar{1}0)_{\text{Mg}} \parallel (01\bar{1})_{\text{Nb}}$ and $[2\bar{1}\bar{1}0]_{\text{Mg}} \parallel [100]_{\text{Nb}}$.

Figure 2 shows three-dimensional structures of the newly formed domain at different strains. It is observed that the nucleus is surrounded by coherent twin boundaries (CTBs), basal–prismatic boundaries (BPs or PBs, $\{0001\} \parallel \{10\bar{1}0\}$), and twist pyramidal–pyramidal boundaries (T-PP1; $\{\bar{1}101\} \parallel \{10\bar{1}\bar{1}\}$). Growth of the subdomain is accomplished through the migration of these interfaces. Atomistic simulations revealed the energies and atomic structures of the three interfaces: the CTB has the formation energy of 125 mJ/m^2 , coherent PBs or BPs have a relatively low formation energy of 105 mJ/m^2 among $\langle 11\bar{2}0 \rangle$ -tilt grain boundaries, and the coherent T-PP1 has the lowest formation energy of 98 mJ/m^2 . The formation of BP/PB and T-PP1 interfaces around the twin nucleus accounts for their low interface energies. Moreover, it is noted that T-PP1 interfaces migrate quickly through the periodic width of the model along the z -axis (Fig. 2b, c) because of a high mobility of TBs on the lateral side.⁴⁴ The subdomain continuously grows via migration of PB interfaces (Fig. 2d). As a result, the nanolayer is reoriented from $\{0001\}$ -oriented to a $\{10\bar{1}0\}$ -oriented interface.

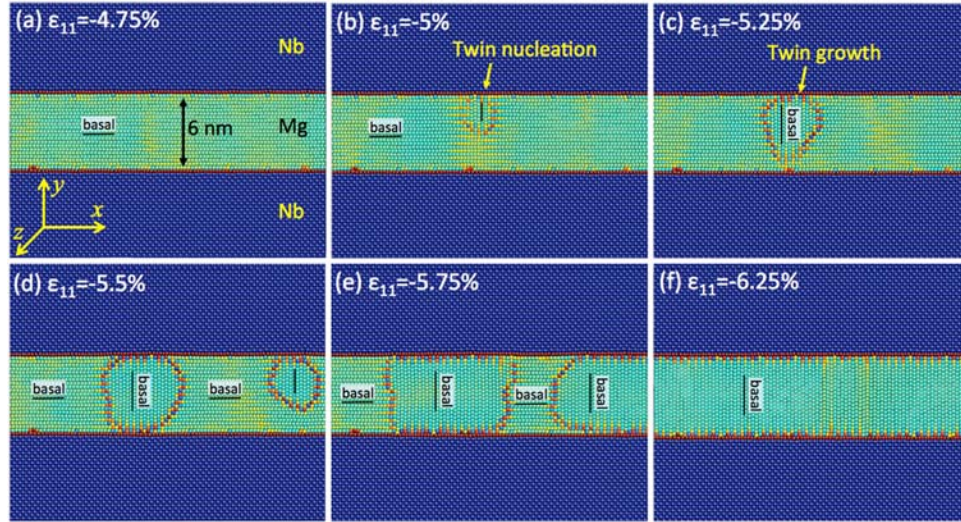


Fig. 1. Nucleation and propagation of subdomains in Mg layer. (a) Before nucleation of subdomains, Mg and Nb layers adopt the orientation relationships $(0001)_{\text{Mg}} \parallel (01\bar{1})_{\text{Nb}}$ and $[2\bar{1}\bar{1}0]_{\text{Mg}} \parallel [100]_{\text{Nb}}$. The compressive load is along the x direction. (b) At $\varepsilon_{11} = -5\%$, a subdomain nucleates from Mg/Nb interface and (c) grows through the thickness. (d) At $\varepsilon_{11} = -5.5\%$, the other subdomain nucleates from interface and (e) both subdomains grow and coalesce. (f) At $\varepsilon_{11} = -6.25\%$, the entire Mg layer is reoriented. The new orientation relationships between Mg and Nb layers becomes $(10\bar{1}0)_{\text{Mg}} \parallel (01\bar{1})_{\text{Nb}}$ and $[2\bar{1}\bar{1}0]_{\text{Mg}} \parallel [100]_{\text{Nb}}$.

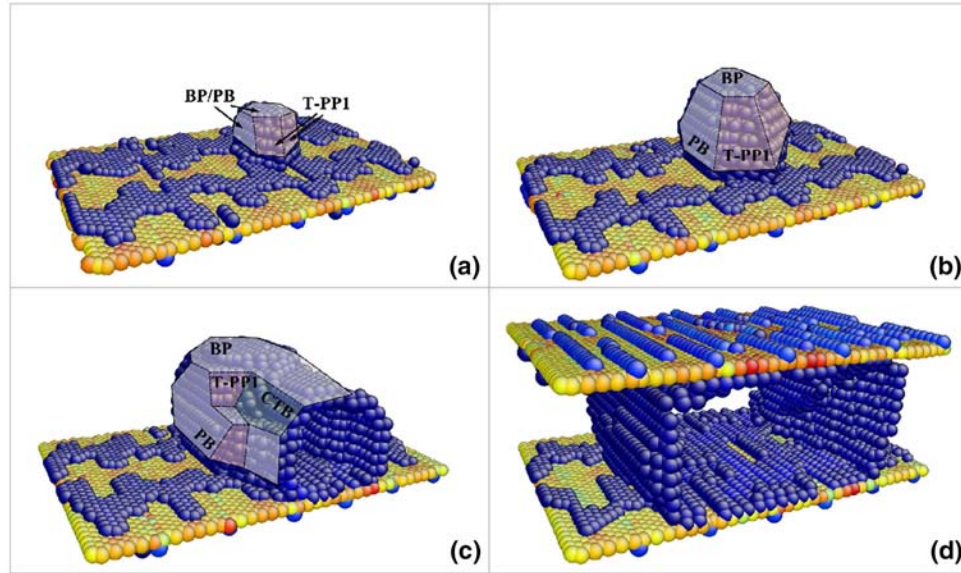


Fig. 2. Snapshots from molecular dynamics simulations showing the formation of a twin subdomain in the Mg phase from a Mg/Nb interface: (a) A twin nucleus nucleates at Mg/Nb interface, (b) the twin nucleus grows via migration of BP/PB and T-PP1 interfaces, (c) and (d) the twin grows through the thickness of the model and continues transverse growth via the migration of PB/BP interfaces.

Figure 3a and c exhibits two cross-sectional atomic structures (in the x - y plane) of the domain at different strains $\varepsilon_{11} = -5\%$ and $\varepsilon_{11} = -5.25\%$. The subdomain is surrounded by BP/PB boundaries and $\{10\bar{1}2\}$ CTBs. Figure 3b and d shows the respective displacements of atoms corresponding to the two structures. Apparently, twinning shear on $\{10\bar{1}2\}$ twin planes cannot cause such displacements, although $\{10\bar{1}2\}$ CTBs form during the nucleation and growth of the subdomain. Compared to the crystallographic orientation of the initial Mg layer, the domain can be considered as a crystal

reorientation through a 90° rotation about the z -axis ($\langle\bar{1}\bar{1}20\rangle$). However, such crystal reorientation is accomplished through atomic shuffling instead of rigid rotation. From a crystallographic viewpoint, the PB or BP boundary corresponds to a 90° rotation of the crystal about the $\langle\bar{1}\bar{1}20\rangle$ direction, while the CTB boundary corresponds to a 86.22° rotation about the $\langle\bar{1}\bar{1}20\rangle$ direction. Recently, atomistic simulations⁴⁵ and in situ mechanical tests in the TEM⁴⁶ revealed that the $\{10\bar{1}2\}$ twin nucleus is surrounded by CTBs, BPs and PBs. Thus, the subdomain is referred to as a ' $\{10\bar{1}2\}$ twin' and

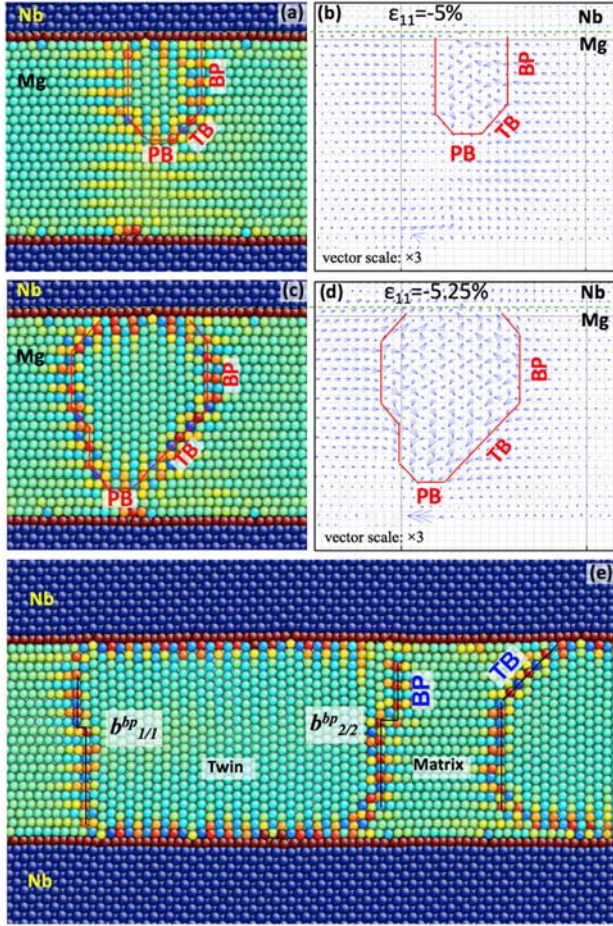


Fig. 3. Twin nucleation process from Mg/Nb interface. (a) Twin nucleus at the incipient stage nucleates from the Mg/Nb interface, consisting of BP/PB boundaries and $\{1012\}$ TBs. (b) The relative displacements of atoms show the atomic shuffling during twinning process. (c, d) The twin grows downward towards the other layer interface by atomic shuffling. (e) Both one-layer ($b_{1/1}^{BP}$) and two-layer disconnections ($b_{2/2}^{BP}$) were observed at BP boundaries during the migration of PB boundaries.

nucleates through pure-shuffle mechanisms. The subdomain grows through the migration of PBs, BPs, and CTBs. The migration of PB boundaries could be achieved via nucleation and glide of a one-layer disconnection^{47,48} or two-layer disconnections,^{49,50} associated with atomic shuffling. In our simulations, both one-layer ($b_{1/1}^{BP}$) and two-layer disconnections ($b_{2/2}^{BP}$) were observed at BP boundaries, as shown in Fig. 3e.

Atomistic simulations revealed that the twins nucleate at the coherent region of the Mg/Nb interface. We characterized the atomic structures of the Mg/Nb interface before and after twin nucleation. The change in interface structure was examined through the displacements of atoms in the 1st and 2nd atomic planes in the Mg layer. Prior to twinning, the equilibrium interface was comprised of three sets of Shockley partial dislocations that divide the interface into six coherent interface regions about an intersection (referred as node) of the three interface dislocations. The six coherent

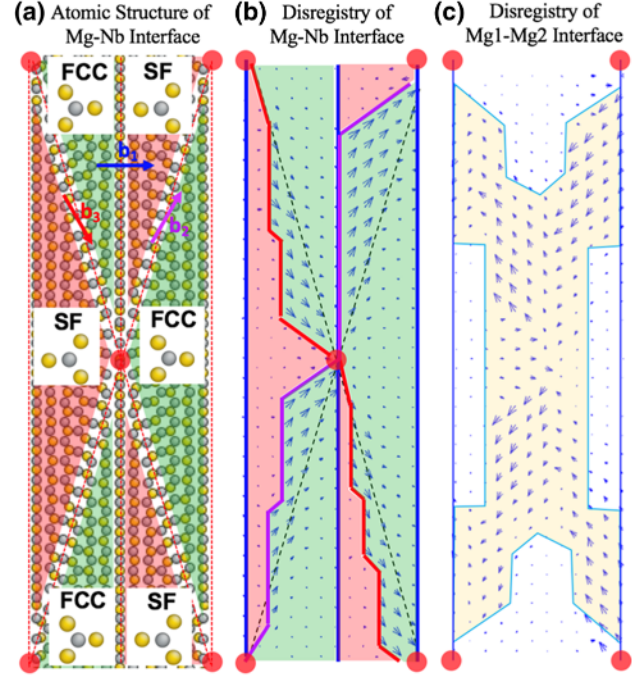


Fig. 4. (a) Atomic structure of Mg/Nb interface, showing coherent interface structures, normal FCC stacking structure (FCC) and intrinsic stacking faulted structure (SF), that are separated by interface misfit dislocations (red dashed lines). (b) The disregistry plot of the Mg/Nb interface at a strain of -4.75% , showing the expansion of the FCC region via the glide of interface dislocations. (c) The disregistry plot of the Mg1-Mg2 interface at a strain of -4.75% , showing atomic shuffling of the 2nd Mg atomic plane (Color figure online).

interface regions take on either a normal FCC structure $[...ABAB]_{Mg}I(CACA...)_{Nb}$ or SF structure $[...ABAB]_{Mg}I(ABAB...)_{Nb}$ based on the stacking sequence across the interface, where “I” represents the interface plane.³⁵ The three interface dislocations have the Burgers vectors, b_1 , b_2 and b_3 , in Fig. 4a, with respect to a reference coherent structure.³⁵ Compared to the interface structure before twinning, the nucleation site corresponds to a FCC coherent region. Using the equilibrium Mg/Nb interface as reference, we characterized the disregistry of the interface before twinning at a strain of -4.75% , showing localized shear associated with the glide of interface dislocations, as shown in Fig. 4b. Noticeably, the glide of interface dislocations is accompanied by the reduction of the SF coherent structure, resulting in the expansion of the FCC coherent structure. Figure 4c shows the disregistry between the 1st and 2nd atomic planes from the interface in Mg, revealing the displacements of atoms in the 2nd atomic plane with respect to the 1st Mg layer. Accompanying the in-plane shear, atoms in the 1st and 2nd atomic planes also experience shuffle displacements normal to the interface (Fig. 3b, d). As a result, the two atomic planes transform from basal plane to prismatic plane, serving as a first two-layer nucleus.

Such prismatic-basal transformation associated with a lattice rotation of 90° results in the reduction of elastic energy in Mg layers under uniaxial compression conditions. There are two transformation strains, one is a compressive strain $\varepsilon_{xx} = -2(\kappa - \sqrt{3})/(\kappa + \sqrt{3})$ and the other is a tensile strain $\varepsilon_{yy} = -\varepsilon_{xx}$, where ε_{xx} is the strain associated with the transformation from the prismatic plane to the basal plane, while ε_{yy} is the strain from the basal plane to the prismatic plane. The combination of these two strains is equivalent to twinning shear strains on two co-zone twin planes, and corresponds to pure shear. The nucleation and growth of such a coherent twin domain is thus driven by compression along the x -axis accompanied by tension along the y -axis. Compared to conventional twinning by simple shear, such a twinning process can be understood through rotation partitioning. A conventional $\{10\bar{1}2\}$ CTB can to a large extent be envisioned as a tilt wall of dislocations.⁵¹ The rotation of 86.22° associated with the tilt wall is equally partitioned between the twin and the matrix.^{45,51,52} However, the compliance of the matrix and the adjacent Nb layers prevents this partitioning, and all the rotation is restricted to the twin nucleus with a coherent rotation of 3.78° imposed on the nucleus. This rotation produces small changes in the strain in the nucleus that can, to the first order, be neglected. Thus, the coherent BP or PB boundaries are true twin interfaces with the partitioning removed.

CONCLUSION

Using atomistic simulations, we explored the possible deformation modes of a Mg nanolayer in Nb/Mg/Nb multilayers. The (0001)-oriented Mg layer transforms or re-orientates into a $\{10\bar{1}0\}$ -oriented Mg layer through nucleation and growth of $\{10\bar{1}2\}$ twins by atomic shuffling, (corresponding to a 90° rotation of the crystal about the $\langle\bar{1}120\rangle$ direction), instead of conventional $\{10\bar{1}2\}$ twinning shear (corresponding to a 86.22° rotation about the $\langle\bar{1}120\rangle$ direction). Such a reorientation accommodates in-plane compressive strain and out-of-plane tensile strain. The nucleation of $\{10\bar{1}2\}$ twins is promoted at the interface due to the structural change associated with the glide of interface dislocations. The initial growth of $\{10\bar{1}2\}$ twins is accomplished through the migration of coherent twin boundaries (CTBs), basal-prismatic boundaries (BPs or PBs, $\{0001\}||\{10\bar{1}0\}$), and twist pyramidal-pyramidal boundaries (T-PP1, $\{\bar{1}101\}||\{10\bar{1}\bar{1}\}$), and subsequent lateral twin growth is accomplished through the migration of PB interfaces via nucleation and glide of one-layer and two-layer disconnections on the PB interface associated with atomic shuffling.

ACKNOWLEDGEMENTS

This work was supported by the Nebraska Center for Energy Sciences Research which is a collabora-

tion between the Nebraska Public Power District (NPPD) and the University of Nebraska-Lincoln (UNL).

REFERENCES

1. P.G. Partridge, *Metall. Rev.* 12, 169 (1967).
2. J.W. Christian and S. Mahajan, *Prog. Mater. Sci.* 39, 1 (1995).
3. M. Barnett, *Mater. Sci. Eng. A* 464, 8 (2007).
4. Q. Yu, Z.-W. Shan, J. Li, X. Huang, L. Xiao, J. Sun, and E. Ma, *Nature* 463, 335 (2010).
5. H. Yoshinaga and R. Horiuchi, *Trans. Japan Inst. Metals* 5, 14 (1964).
6. A. Akhtar and E. Teghtsoonian, *Acta Metall.* 17, 1351 (1969).
7. V. Vitek and V. Paidar, *Dislocations in Solids* (2008), vol. 14, p. 439.
8. M. Yoo, *Metall. Trans. A* 12, 409 (1981).
9. P. Cizek and M. Barnett, *Scripta Mater.* 59, 959 (2008).
10. D. Ando, J. Koike, and Y. Sutou, *Mater. Sci. Eng. A* 600, 145 (2014).
11. Q. Yu, J. Wang, Y. Jiang, R.J. McCabe, N. Li, and C.N. Tomé, *Acta Mater.* 77, 28 (2014).
12. A. Jain and S. Agnew, *Mater. Sci. Eng. A* 462, 29 (2007).
13. A.S. Khan, A. Pandey, T. Gnäupel-Herold, and R.K. Mishra, *Int. J. Plast.* 27, 688 (2011).
14. A. Chapuis and J.H. Driver, *Acta Mater.* 59, 1986 (2011).
15. B. Mordike and T. Ebert, *Mater. Sci. Eng. A* 302, 37 (2001).
16. K. Hantzsche, J. Bohlen, J. Wendt, K. Kainer, S. Yi, and D. Letzig, *Scripta Mater.* 63, 725 (2010).
17. M. Furukawa, Z. Horita, M. Nemoto, R. Valiev, and T. Langdon, *Acta Mater.* 44, 4619 (1996).
18. K. Kubota, M. Mabuchi, and K. Higashi, *J. Mater. Sci.* 34, 2255 (1999).
19. M. Barnett, Z. Keshavarz, A. Beer, and D. Atwell, *Acta Mater.* 52, 5093 (2004).
20. T. Al-Samman and X. Li, *Mater. Sci. Eng. A* 528, 3809 (2011).
21. S. Yi, J. Bohlen, F. Heinemann, and D. Letzig, *Acta Mater.* 58, 592 (2010).
22. Y. Kawamura, K. Hayashi, A. Inoue, and T. Masumoto, *Mater. Trans.* 42, 1172 (2001).
23. E. Abe, Y. Kawamura, K. Hayashi, and A. Inoue, *Acta Mater.* 50, 3845 (2002).
24. X. Shao, Z. Yang, and X. Ma, *Acta Mater.* 58, 4760 (2010).
25. A. Misra, J. Hirth, and R. Hoagland, *Acta Mater.* 53, 4817 (2005).
26. J. Wang, R. Hoagland, J. Hirth, and A. Misra, *Acta Mater.* 56, 5685 (2008).
27. A. Misra and R. Hoagland, *J. Mater. Sci.* 42, 1765 (2007).
28. A. Misra, M. Verdier, Y. Lu, H. Kung, T. Mitchell, M. Nastasi, and J. Embury, *Scripta Mater.* 39, 555 (1998).
29. T.M. Pollock, *Science* 328, 986 (2010).
30. J. Wang and A. Misra, *Curr. Opin. Solid State Mater. Sci.* 15, 20 (2011).
31. J. Carpenter, T. Nizolek, R. McCabe, S. Zheng, J. Scott, S. Vogel, N. Mara, T. Pollock, and I. Beyerlein, *Mater. Res. Lett.* 3, 50 (2015).
32. B. Ham and X. Zhang, *Mater. Sci. Eng. A* 528, 2028 (2011).
33. S. Pathak, N. Velisavljevic, J.K. Baldwin, M. Jain, S. Zheng, N.A. Mara, and I.J. Beyerlein, *Sci. Rep.* 7, 8264 (2017).
34. A. Kumar, I.J. Beyerlein, and J. Wang, *Appl. Phys. Lett.* 105, 071602 (2014).
35. Y. Chen, S. Shao, X.-Y. Liu, S.K. Yadav, N. Li, N.A. Mara, and J. Wang, *Acta Mater.* 126, 552 (2017).
36. S.K. Yadav, S. Shao, Y. Chen, J. Wang, and X.-Y. Liu, *J. Mater. Sci.* 53, 5733 (2018).
37. J. Koike, T. Kobayashi, T. Mukai, H. Watanabe, M. Suzuki, K. Maruyama, and K. Higashi, *Acta Mater.* 51, 2055 (2003).
38. S.R. Agnew and Ö. Duygulu, *Int. J. Plast.* 21, 1161 (2005).
39. X.-Y. Liu, J.B. Adams, F. Ercolessi, and J.A. Moriarty, *Model. Simul. Mater. Sci. Eng.* 4, 293 (1996).
40. G. Ackland and R. Thetford, *Philos. Mag. A* 56, 15 (1987).

41. W.G. Hoover, *Phys. Rev. A* 31, 1695 (1985).
42. S. Nosé, *J. Chem. Phys.* 81, 511 (1984).
43. R. Zhang, J. Wang, I. Beyerlein, and T. Germann, *Scripta Mater.* 65, 1022 (2011).
44. M. Gong, G. Liu, J. Wang, L. Capolungo, and C.N. Tomé, *Acta Mater.* 155, 187 (2018).
45. J. Wang, S. Yadav, J. Hirth, C. Tomé, and I. Beyerlein, *Mater. Res. Lett.* 1, 126 (2013).
46. B.-Y. Liu, J. Wang, B. Li, L. Lu, X.-Y. Zhang, Z.-W. Shan, J. Li, C.-L. Jia, J. Sun, and E. Ma, *Nat. Commun.* 5, 3297 (2014).
47. A. Ostapovets and A. Serra, *Philos. Mag.* 94, 2827 (2014).
48. B. Xu, L. Capolungo, and D. Rodney, *Scripta Mater.* 68, 901 (2013).
49. J. Wang, L. Liu, C. Tomé, S. Mao, and S. Gong, *Mater. Res. Lett.* 1, 81 (2013).
50. C.D. Barrett and H. El Kadiri, *Acta Mater.* 63, 1 (2014).
51. J. Hirth, J. Wang, and C. Tomé, *Prog. Mater. Sci.* 83, 417 (2016).
52. J. Hirth, R. Pond, R. Hoagland, X.-Y. Liu, and J. Wang, *Prog. Mater. Sci.* 58, 749 (2013).

Publisher's Note Springer Nature remains neutral with regard to jurisdictional claims in published maps and institutional affiliations.